SUMMARY OF STRUCTURAL ALLOY COMPATIBILITY IN SUPERCRITICAL CO_2 AT 450°-800°C

Bruce A. Pint, Rishi Pillai and James R. Keiser
Materials Science & Technology Division, Oak Ridge National Laboratory, Oak Ridge, TN USA

ABSTRACT

Supercritical CO_2 (sCO_2) is of interest as a working fluid for several concepts including the direct-fired Allam cycle as a low-emission fossil energy power cycle. Over the past 10 years, laboratory exposures at 300 bar sCO_2 have found reasonably good compatibility for Ni-based alloys at ≤800°C, including an assessment of the sCO_2 impact on room temperature mechanical properties after 750°C exposures. However, initial screening tests at 1 and 20 bar CO_2 at 900°-1100°C showed poor compatibility for Ni-based alloys. In an open cycle, the introduction of 1%O_2 and 0.1-0.25%H_2O impurities at 300 bar increased the reaction rates ≥2X at 750°C. At lower temperatures, steels are susceptible to C ingress and embrittlement. Creep-strength enhanced ferritic steels may be limited to <550°C and conventional stainless steels to <600°C. Two strategies to increase those temperatures are higher Ni and Cr alloying additions and Al- or Cr-rich coatings. Alloy 709 (Fe-20Cr-25Ni) shows some promising results at 650°C in sCO_2 but reaction rates were accelerated with the addition of O_2 and H_2O impurities. Pack aluminized and chromized Gr.91 (Fe-9Cr-1Mo) and type 316H stainless steel show some promise at 600°-650°C but further coating optimization is needed.

INTRODUCTION

In the search for clean, dispatchable power generation, the direct-fired or open supercritical CO_2 (sCO_2) Allam cycle is a potentially economical, zero-emission electricity source from fossil fuels [1,2]. Indirect or closed sCO_2 cycles also can be attractive for nuclear, concentrating solar power (CSP), geothermal, and waste heat recovery applications [3-7] as the unique sCO_2 physical properties enable high efficiencies [8]. Ten years ago, there was a significant concern about structural material compatibility to enable sCO_2 cycles at >700°C and >50% cycle efficiency, especially with the O_2 and H_2O impurities in the Allam cycle. Since then, several studies found good compatibility of Ni-based alloys in sCO_2 [9-16], even with impurities present [17-20]. Nevertheless, sCO_2 has a low critical point (31°C/74 bar) so a sizable portion of the cycle operates at <650°C. To be commercially competitive, lower cost Fe-based materials are needed at these lower temperatures. However, there is a significant historical concern about steels exposed to CO_2 environments [21] dating back to the severe internal carburization observed in Grade 9 (Fe-9Cr-1Mo) steel in the UK advanced gas cooled reactors (AGRs) operated with sub-critical 43 bar CO_2 at <550°C [22]. More recent sCO_2 studies have concluded that 9-12%Cr ferritic-martensitic (FM), or creep-strength enhanced ferritic (CSEF) steels are limited to 450°C in sCO_2 [23] and conventional austenitic stainless steels begin to show accelerated attack in sCO_2 at ~600°C [9,23-27]. These are lower temperature limits than supercritical steam [28-30] and it increases the need for more expensive Ni-based alloys if this issue cannot be addressed.

A recently concluded, multi-year experimental program focused on determining the maximum use temperature of CSEF and austenitic steels in sCO_2 with and without O_2 and H_2O impurities at 450°-650°C [20,27,31-34]. Two strategies were investigated to increase the sCO_2 temperature limit. For austenitic steels, increasing the Cr and Ni contents appears to improve sCO_2 compatibility. Also, initial results on Cr- and Al-rich coatings on lower alloyed steels builds upon prior work in steam and CO_2 [35-42]. Initial exposures at 650°C in sCO_2 revealed some limitations of coatings, especially with impurities [32-34]. Subsequent work at 600°C is the focused of these results.

EXPERIMENTAL PROCEDURES

The measured chemical compositions of the exposed materials are shown in Table 1. Specimen coupons (~12 x 20 x 1.5mm) and dogbone tensile specimens (SS-3 type: 25.4 mm long, 0.76 x 5 mm gauge, 0.7mm thickness) were prepared to a 600-grit finish and ultrasonically cleaned in acetone and methanol prior to exposure. Exposures in 500-h cycles were conducted in research grade (RG) sCO_2 (<5 ppm O_2, <5 ppm H_2O) in a vertically-oriented autoclave (~266 mm x 83 mm inner diameter). Both autoclave and specimen rack were made from alloy 282. A 3-zone furnace heated the autoclave to the hold temperature (±2°C) over several hours (~2°C/min) with 300 bar sCO_2 (~2 ml/min) present during heating and cooling. For the controlled impurity experiments [18,20], individual pumps for H_2O and sCO_2 were used, while O_2 was added as a CO_2–O_2 gaseous mixture from a high-pressure cylinder. The O_2 was calculated as 1.0 ± 0.2% and the H_2O content as 0.1 ± 0.05% based on gas flow rates with the largest variations associated with issues with filters, valves and changing sCO_2 cylinders (usually twice per 500-h cycle).

Subcritical RG CO_2 exposures were conducted using 500-h cycles in the "Keiser" test rig [43,44] with parallel Hexoloy (SiC) containment tubes and the specimens held on a vertical alumina tube using alumina rods through holes in the coupons. The specimens were slowly heated to temperature in argon and then exposed to the same RG CO_2 gas (typical vendor measured H_2O content of 4.1±0.7 ppm) with one tube at 1 bar and the second at 20 bar total pressure.

Table 1: Alloy compositions measured by inductively coupled plasma and combustion analyses

Alloy	Fe	Cr	Ni	Mo	Mn	Si	C	S*	Other
Gr.91	88.8	8.6	0.3	0.9	0.46	0.35	0.10	6	0.2V,0.06Nb,0.045N
VM12	83.3	11.5	0.4	0.4	0.4	0.4	0.12	3	1.6W,1.5Co,0.2V,0.04N
316H	69.5	16.3	10.0	2.0	0.84	0.46	0.041	6	0.3Cu,0.3Co,0.04N
709	51.3	20.1	25.2	1.5	0.89	0.41	0.064	3	0.2Nb,0.06Cu,0.15N
304H	70.0	18.3	8.6	0.3	1.8	0.3	0.07	51	0.4Cu,0.2Co,0.06
310HN	51.3	25.5	20.3	0.1	1.2	0.3	0.05	4	0.3Co,0.4Nb,0.3N
25SS	42.6	22.3	25.4	0.2	0.5	0.2	0.07	8	3.4W,3Cu,1.5Co,0.5Nb
825	30.8	22.7	39.5	3.0	0.55	0.35	0.02	<5	1.7Cu,1.0Ti,0.2Al,0.02Hf
625	4.0	21.7	61.0	8.8	0.2	0.2	0.02	<3	4Fe,3.5Nb,0.2Ti,0.1Al
230	1.5	22.6	60.5	1.4	0.5	0.4	0.10	9	12.3W,0.3Al
693	4.8	28.6	62.1	0.03	0.19	0.05	0.03	<3	3.1Al,0.6Nb,0.4Ti
740H	0.1	24.5	49.7	0.3	0.3	0.2	0.03	17	21Co,1.5Nb,1.4Ti,1.4Al
282	0.2	19.6	57.1	8.6	0.02	0.04	0.06	<3	10.6Co,2.2Ti,1.6Al
738	0.03	16.5	60.8	1.7	<	0.01	0.01	3	8.6Co,3.4Ti,3.7Al,2.6W,1.8Ta
247	0.07	8.5	59.5	0.7	<	0.03	0.16	<3	10Co,10W,3Ta,6Al,1.4Hf
X4	0.05	6.4	60.8	0.6	<	0.02	0.004	<3	10Co,7Ta,6W,3Re,1Ti,.08Hf

* S in ppmw < signifies less than 0.002

The specimens were weighed before and after exposure using a Mettler Toledo model XP205 balance with an accuracy of ±0.04 mg. Room-temperature tensile tests used a strain rate of 0.015/min per ASTM E8-13. Bulk carbon contents were measured using combustion analysis. For metallography, specimens with thin reaction products were copper plated before being sectioned. Polished sections were then characterized using light microscopy and secondary electron microscopy (SEM) equipped with energy dispersive x-ray spectroscopy (EDS), using a TESCAN model MIRA3. Creep and creep-fatigue testing was performed on seamless tubing where the walls were thinned to allow rupture in a reasonable time. End caps were welded onto tube segments that were pressurized and exposed at 750°C until rupture.

RESULTS AND DISCUSSION

Figure 1 summarizes the rate constants generated from the 2-20 median mass gain data points (after 2-20 500-h cycles) from 4-10 specimens of each alloy at each condition. The rate constants were generated using a standard method [45] and are compared to values from the literature in sCO_2 without impurities [11,14] shown as small circles. A metric developed for CSP applications [16] is shown as a horizontal dashed line in Figure 1. The Ni-based alloys shown here, 625, 282 and 740H, all meet the metric up to 800°C (the limit of 300 bar sCO_2 autoclave testing). While many of the conventional Fe-based alloys showed higher rates at 600°-650°C

At 800°C, only 2 cycles were run on specimens and Figure 2 provides examples of some of the scales formed under these conditions. As noted previously, Al and Ti internally oxidized beneath the Cr-rich oxide formed on alloys like 282 and 740H, but this is similar to behavior in 1 bar CO_2 and laboratory air [16]. Two examples are shown in Figure 2a to emphasize that similar results were obtained for specimens run in 2016 and 2022. With low levels of Al and Ti (Table 1), alloy 625 forms a thinner scale. The higher Al levels in superalloys 247 and X4 can result in thinner surface oxides and less internal oxidation, Figures 2c and 2f. Finally, alloy 825 is expected to be less expensive because it contains >30%Fe (Table 1) and none of the expensive alloying elements like Co and Mo. Nevertheless, it formed an oxide similar in thickness to other Ni-based alloys, Figure 2e. The Cu plating shown in Figure 2 is used to protect the reaction product, however, it can separate from the specimen and make the oxide appear thicker. The gap between the Cu plating and oxide is noted in Figure 2e.

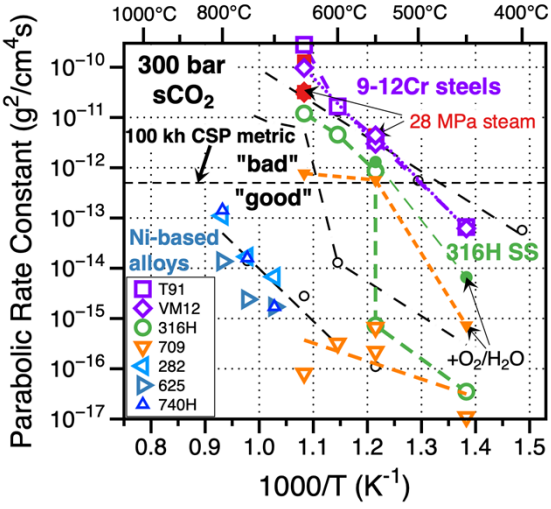

Figure 1: Arrhenius plot of literature values (small circles)[11,14] and rate constants in 300 bar RG sCO_2 (open symbols)[16,27] and RG sCO_2+1%O_2+0.1%H_2O (solid symbols) [20,33].

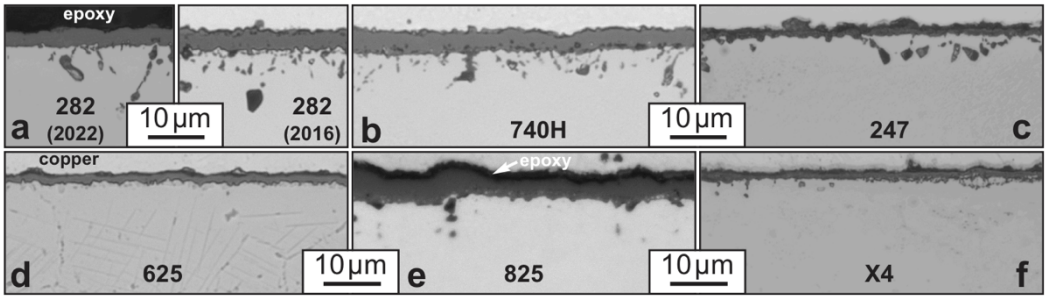

Figure 2: Light microscopy of polished sections of alloy specimens exposed for 1,000 h at 800°C in RG sCO2: (a) 282 (examples from specimens run in 2016 and 2022), (b) 740H, (c) 247, (d) 625, (e) 825 and (f) single crystal superalloy X4.

Figure 3a summarizes mechanical testing performed at 750°C on pressurized tube specimens tested to failure with either air or sCO_2 inside. The Larson Miller Parameter (LMP) captures the time and temperature of the creep tests. After initially testing 740H specimens over a large range of stresses, the other alloys were subsequently tested only at lower stresses for longer times. For all the alloys tested, there was no statistically significant debit for creep testing with sCO_2 compared to testing with air, Figure 3a. The higher stresses used for alloys 740H and 282 reflect the higher strength of these alloys compared to alloy 625 and the Sandvik stainless steel alloy 25. To capture the cyclic nature of the application, Figure 3b shows creep-fatigue results for pressurized 740H tube specimens tested with air and sCO_2. Each 8 min cycle consisted of pressurizing to 410 bar, a 6 min hold and then depressurizing, while the specimen was held at 750°C. For this material under these conditions, there appeared to be a debit in fatigue lifetime in sCO_2 compared to air. The lifetime had been calculated to be 3,000 cycles under these conditions and only tests with sCO_2 failed to meet that lifetime.

Figure 4 shows mass change from subcritical testing of several Ni-based alloys at temperatures of 900°-1100°C in laboratory air and 1 and 20 bar RG CO_2 [46]. The sCO_2 autoclave is not capable of temperatures above 800°C. Unlike the 700°-800°C sCO_2 results, the 1 and 20 bar CO_2

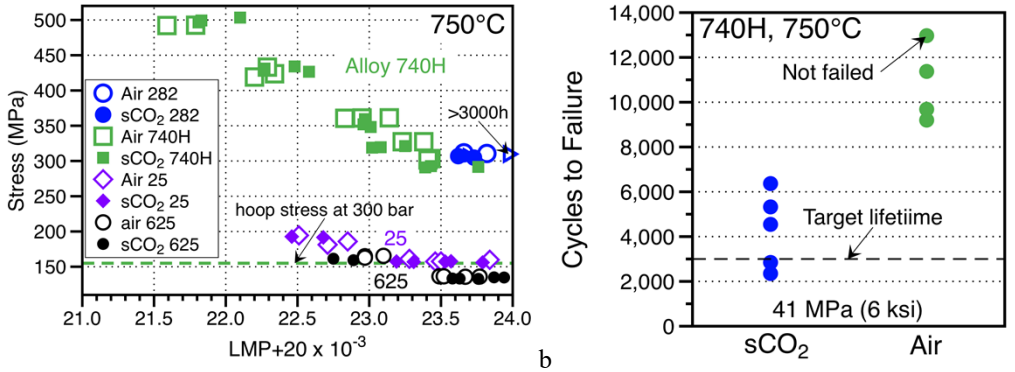

Figure 3: (a) Larson Miller Parameter (LMP) calculated for each rupture versus the applied hoop stress is shown for the sCO_2 and pressurized air experiments at 750°C. Since the 625 and 25 specimens overlapped, an offset is used to clearly show the data. The hoop stress at 300 bar is shown for the wall thickness of the alloy 740H specimens. (b) Cycles to failure for 740H tube specimens pressurized at 750°C with air or CO_2. Each cycle consisted of a 6 min hold at 410 bar.

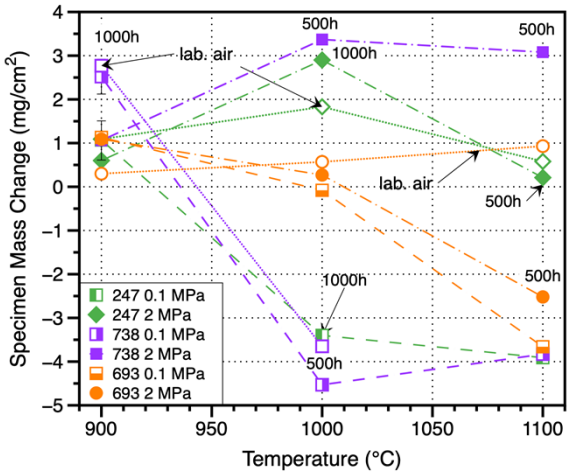

Figure 4. Specimen mass change data for alloy specimens exposed to air (open symbols), RG CO_2 in 1 bar (half symbols) and 20 bar (closed symbols) as a function of exposure temperature. All of the 900°C exposures were 1000 h but 500 h exposures were used at higher temperatures when large mass changes were observed [46].

environment led to enhanced mass gains and losses with the formation of Ni-rich oxides (i.e. less protective scales) and spallation, especially at 1100°C [46]. While the behavior has not been fully explored as to the reason for the degradation in CO_2, the temperature window for using Ni-based alloys appears to be finite.

Regarding the effect of O_2 and H_2O impurities in sCO_2 relevant to the Allam cycle [1,2], Figure 5 shows a comparison of Fe- and Ni-based alloy specimen mass gains in different 300 bar environments compared to laboratory air after 1000 h at 750°C [20]. The impurity levels (e.g. 18 ± 16 ppm H_2O measured in 10 gas cylinders [16]) in industrial grade (IG) sCO_2 did not significantly change the median mass change compared to RG sCO_2. To simulate the Allam cycle, the O_2 additions were 1% and the H_2O additions were 0.25% to reflect the portion of the cycle after the H_2O is dropped out before the sCO_2 returns to the combustor. The Fe-based alloys were strongly affected by impurities, with the lowest alloyed steel, type 304H (Table 1) having large mass gains and losses depending on the Fe-rich oxide adhesion. Comparing when the 1%O_2 and 0.25%H_2O

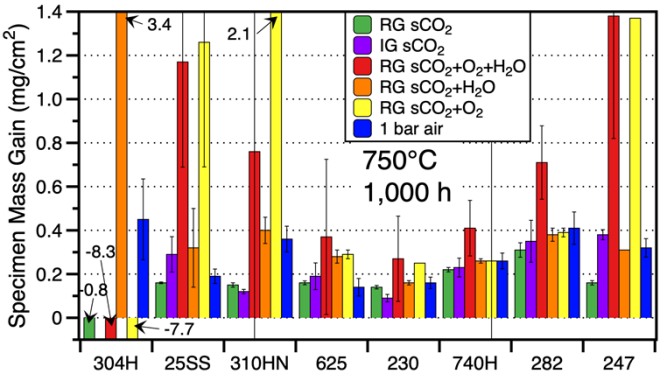

Figure 5. Median mass gain of specimens in various environments after 1000 h at 750 °C. Based on [20].

were added individually, all the steels, 304H, 25SS (Sanicro 25) and 310HN (310HCbN or HR3C)) were more strongly attacked (more Fe-rich oxide formation) by the sCO_2+1%O_2 environment, with similar mass changes as the sCO_2+1%O_2+0.25%H_2O environment, Figure 5. The Ni-based alloys were not as strongly affected by the impurity additions except for the low Cr superalloy 247 (i.e. MarM247), where higher mass gains were measured when O_2 was present with or without H_2O due to the formation of a less protective oxide scale [18].

The more recent test matrix focused on steels and the effect of 1%O_2 and 0.1%H_2O impurities. Returning to Figure 1, the rates for the FM/CSEF steels were high above 500°C and little benefit was observed for the higher Cr content in VM12 compared to T91, Table 1, under these conditions. As has been observed previously [23-25], FM steels form duplex Fe-rich scales in sCO_2 and the results have been reported previously [18,20,34]. However, it should be noted that the rates observed for these FM steels are similar to those measured in 276 bar H_2O [47], Figure 1.

For the stainless steels, thin oxides formed at 450°C in RG sCO_2 for both 316H and 709 with correspondingly very low reaction rates, Figure 1. The rates for 709 in RG sCO_2 continued to be low up to 650°C, comparable to the rates for Ni-based alloys. For 316H specimens, a transition occurred at 550°-600°C where a thin Cr-rich oxide could no longer be formed in RG sCO_2. The formation of Fe-rich oxides corresponded to a significant increase in the reaction rate, nearly as high as the FM steels, Figure 1. The addition of O_2 and H_2O impurities at 450°C increased the oxide scale thickness and the rate (closed symbols in Figure 1) at 450°C, but still below the parabolic rate constant metric. At 550° and 650°C, the rates jumped above the metric due to more significant Fe-rich oxide formation. While this acceleration occurred for 316H specimens without impurities, this was a significant change for the 709 specimens. In Figure 6, it is noted that these rates are affected by a significant mass gain increase after 500 h for the 5 alloy 709 specimens exposed for 1000 h at 550° and 650°C. While two data points may have been sufficient to calculate rates without impurities [16], this may not be the case with impurities and experiments are in progress to continue the 650°C experiment to longer times to calculate more accurate rates for alloy 709. Figure 6 shows more modest mass gains between 1000 and 2000 h at 650°C.

To illustrate the effect of impurities on the scale thickness, Figure 7 shows images of the scales formed on 316H and 709 at 550°C and the similar increase in oxide thickness for alloy 709 specimens exposed at 650°C. At both temperatures, transitioning from a thin Cr-rich oxide formed

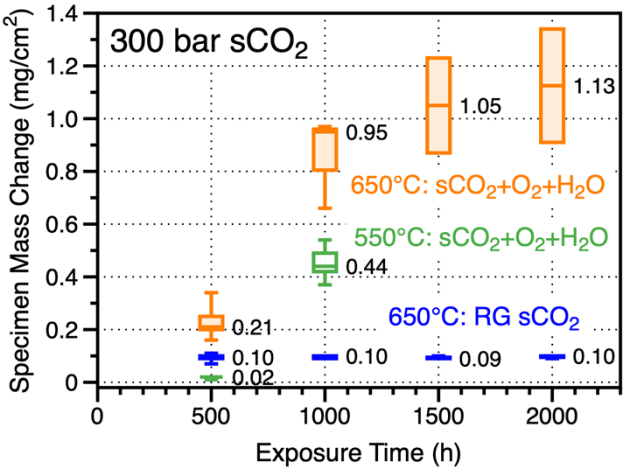

Figure 6. Box and whisker plot of specimen mass change in 500-h cycles for 709 specimens exposed in RG sCO_2 with and without 1%O_2+0.1%H_2O at 550° and 650°C.

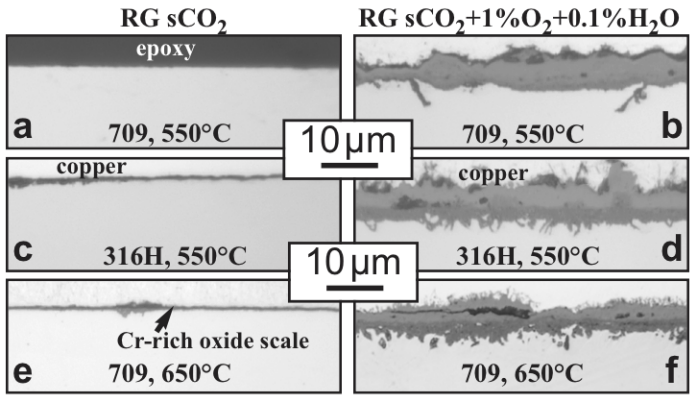

Figure 7. Light microscopy of polished cross-sections of (a,b,e,f) 709 and (c,d) 316H exposed for 1000 h at (a-d) 550°C and (e-f) 650°C in (a,c,e) RG sCO_2 & (b,d,f) RG sCO_2+1%O_2+0.1%H_2O.

in RG sCO_2 to a duplex oxide with significant Fe-rich oxide formation after 1000 h [20]. The light microscopy in Figure 7 differentiates the darker $(Fe,Cr)_3O_4$ inner oxide layer from the lighter Fe_2O_3 outer layer that forms with the addition of 1%O_2. In RG sCO_2, the Fe-rich oxide formed was Fe_3O_4.

While mass gain is one metric, an important issue is C ingress due to the C gradient across the scale [48] and its impact on mechanical properties [13,20,27,31-34,49]. Figure 8 plots the room temperature elongation vs. the specimen mass gain. As reported previously [20,27,32], 316H tensile specimens showed a dramatic drop in ductility at 650°C with and without impurities. In contrast, the ductility of alloy 709 specimens was unaffected by RG sCO_2 after 500 and 1000 h exposures. However, with the addition of impurities and the formation of Fe-rich oxides at 650°C, a drop in ductility was observed at 650°C, Figure 8. In other materials, C ingress could be tracked by measuring the bulk C content in alloy coupons after sCO_2 exposures, Figure 9. However, no significant increase in the bulk C content of 709 specimens was measured after 1,000 h. Using glow discharge optical emission spectroscopy, an increase in C was measured at the surface of a

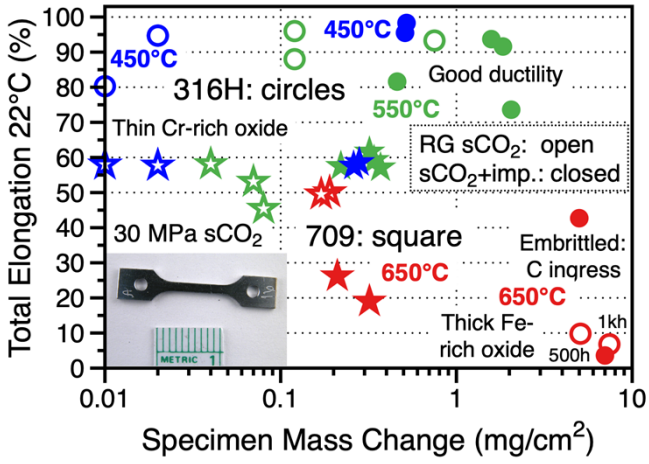

Figure 8. Mass change of 316H and 709 specimens plotted versus post-exposure room temperature total elongation for 500-2000 h exposures in 300 bar RG sCO_2 (open symbols) and RG sCO_2+1%O_2+0.1%H_2O (closed symbols). Compiled data [X]

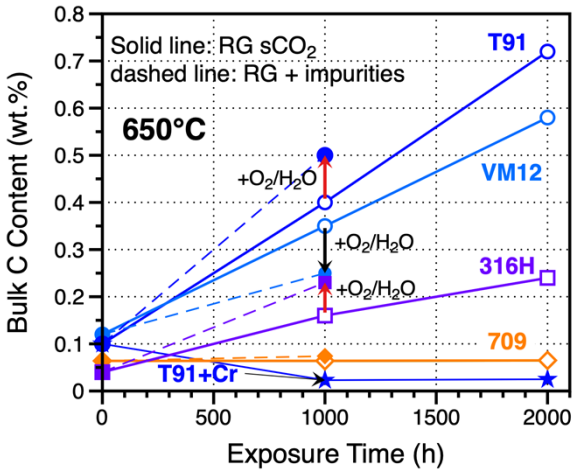

Figure 9. Bulk C content measured as a function of exposure time in sCO_2, closed symbols at 650°C and open symbols at 550°C; solid lines in RG sCO_2 and dashed lines with impurities.

709 specimen exposed for 1000 h to sCO_2 with impurities [20]. It is possible that longer exposures would discover C ingress for alloy 709 specimens exposed to RG sCO_2 at 650°C or lower temperatures. Exposures to 2000 h show no increase in mass gain, Figure 6, or increase in bulk C content, Figure 9.

While increasing the Cr and Ni contents of steels is one strategy to improve sCO_2 compatibility, another strategy is coatings. The current study included pack Cr and Al coatings on T91 and 316H substrates and the mass change results at 600° and 650°C are reported in Figure 10. The 650°C results have been reported previously [32-34]. The Cr-coated specimens had much lower mass gains than bare alloys in RG sCO_2 at 650°C but the coatings were less protective when 1%O_2 and 0.1%H_2O impurities were added to the test environment, Figure 10b. An Al pack coating on T91 did not form an Al-rich oxide in either environment. The focus here is on results at 600°C in RG sCO_2 to see if decreasing the temperature would improve coating performance, Figure 10a. Again, the pack Cr coating appeared to be more protective. However, the EDS maps in Figure 11 suggest that Cr-rich carbides are forming in the coating on 316H. The formation of carbides in the coating reduces the Cr reservoir to form a protective Cr-rich oxide. Also, the EDS line profile in Figure 12a shows that the coating was only ~15 µm thick using a commercial process.

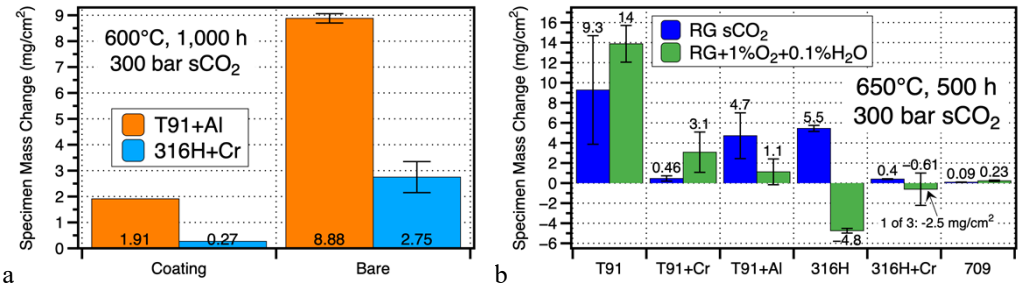

Figure 10. Specimen mass gains (a) 1000 h at 600°C in RG sCO_2 and (b) 500 h at 650°C in RG sCO_2 with and without impurities [34]. The whiskers show one standard deviation of the average when multiple specimens were exposed.

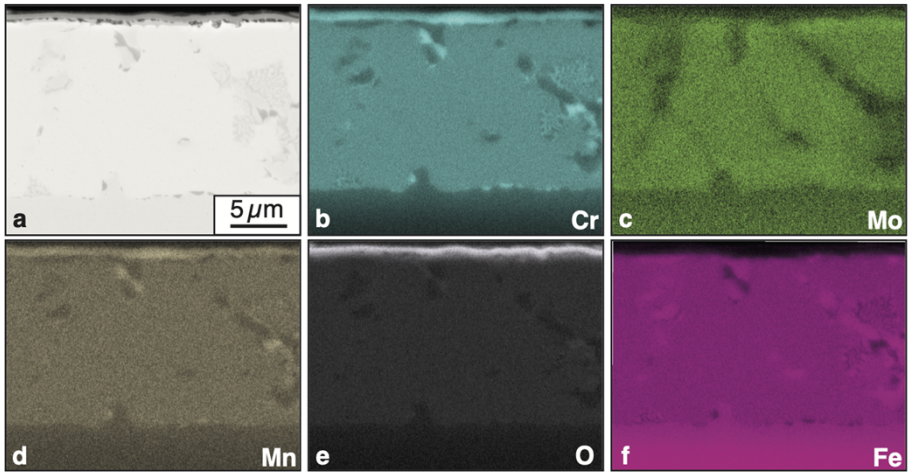

Figure 11. (a) SEM secondary electron image of the near surface area of a chromized 316H specimen exposed to RG sCO_2 at 600°C for 1000 h and (b-f) associated EDS maps from (a).

Figure 10a suggests less benefit for an Al pack coating on T91. The line profile in Figure 12b shows that the surface oxide is enriched in Al but contains a significant amount of Fe. The pack coating parameters targeted a relatively thin, ~100 µm coating with a peak Al content of ~20 wt.% Al to minimize the formation of Fe-Al intermetallics [35]. However, this Al level appeared to be insufficient to form a highly protective Al_2O_3 surface oxide layer. For both the pack Al and Cr coatings, more optimization appears to be necessary to get more protective behavior in sCO_2.

CONCLUSIONS

A selection of results was presented on the compatibility of Fe- and Ni-based alloys in sCO_2. Ni-based alloys appear to be compatible with 300 bar sCO_2 at ≤800°C with thin reaction products, low reaction rates and minimal impact on mechanical properties. At 750°C, even the introduction of 1%O_2 and 0.25%H_2O impurities at 300 bar had limited impact. However, at 900°-1100°C, more attack was noted in 1 and 20 bar RG CO_2. Ferritic and austenitic steels were investigated at 450°-650°C with and without impurities. An advanced austenitic steel like alloy 709 showed significantly better compatibility with lower reaction rates and no loss of room temperature

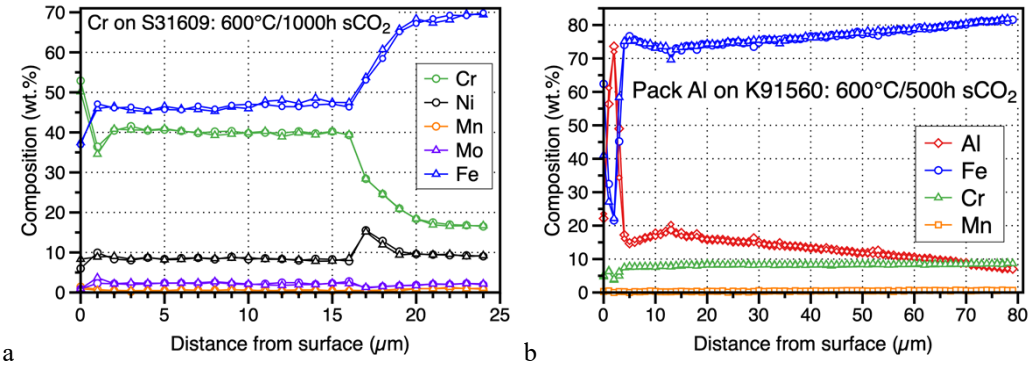

Figure 12. EDS line profiles of the coatings exposed in RG sCO_2 at 600°C (a) aluminized T91 after 500 h and (b) chromized 316H after 1,000 h.

ductility in RG sCO_2. However, the addition of $1\%O_2$ and $0.1\%H_2O$ impurities did increase the reaction rate and showed signs of loss of room temperature ductility. Initial results for pack Al and Cr coatings suggested some promise at 600°-650°C but further coating optimization is needed.

ACKNOWLEDGMENTS

The authors would like to thank B. Johnston, T. M. Lowe and D. Newberry for assistance with the experimental work at ORNL. The creep testing was performed at Brayton Energy, LLC by J. Nash and J. Kesseli, and the Al pack coating was performed by Prof. Y. Zhang at Tennessee Technological University. Haynes International provided alloys 282 and 625, Special Metals provided 740H and Sandvik provided alloy 25, Y. Wang at ORNL provided 709, EPRI provided VM12 and Tenaris provided the Grade 91 material. M. Ridley and J. Jun at ORNL provided helpful comments on the manuscript. This research was sponsored by the U.S. Department of Energy, Office of Fossil Energy and Carbon Management, Advanced Materials Program.

REFERENCES

[1] Allam, R. J., Palmer, M. R., Brown Jr., G. W., Fetvedt, J., Freed, D., Nomoto, H., Itoh, M., Okita, N., Jones Jr., C., "High efficiency and low cost of electricity generation from fossil fuels while eliminating atmospheric emissions, including carbon dioxide," *Energy Procedia*, Vol. 37, (2013), pp. 1135–1149.

[2] Allam, R., Martin, S., Forrest, B., Fetvedt, J., Lu, X., Freed, D., Brown, Jr., G. W., Sasaki, T., Itoh, M., Manning, J., "Demonstration of the Allam Cycle: An Update on the Development Status of a High Efficiency Supercritical Carbon Dioxide Power Process Employing Full Carbon Capture," *Energy Procedia*, Vol. 114, (2017), pp. 5948-5966.

[3] Dostal, V., Hejzlar, P., Driscoll, M. J., 2006, "The supercritical carbon dioxide power cycle: Comparison to other advanced power cycles," *Nuclear Technology*, Vol. 154(3), (2006), pp. 283-301.

[4] Chen, H., Goswami, D. Y., Stefanakos, E. K., "A review of thermodynamic cycles and working fluids for the conversion of low-grade heat," *Renewable & Sustainable Energy Reviews*, Vol. 14, (2010), 3059-3067.

[5] Iverson, B. D., Conboy, T. M., Pasch, J. J., Kruizenga, A. M., 2013, "Supercritical CO_2 Brayton cycles for solar-thermal energy," *Applied Energy*, Vol. 111, (2013) 957-970

[6] Wright, I. G., Pint, B. A., Shingledecker, J. P., Thimsen, D., 2013, "Materials Considerations for Supercritical CO2 Turbine Cycles," ASME Paper #GT2013-94941, presented at the International Gas Turbine & Aeroengine Congress & Exhibition, San Antonio, TX, June 3-7, 2013.

[7] Cheang, V., Hedderwick, R. A, McGregor, C., "Benchmarking supercritical carbon dioxide cycles against steam Rankine cycles for Concentrated Solar Power," *Solar Energy*, Vol. 113, (2015), 199-211.

[8] Feher, E. G., "The Supercritical Thermodynamic Power Cycle," *Energy Conversion*, Vol. 8, (1968), pp. 85-90.

[9] Olivares, R. I., Young, D. J., Marvig, P., Stein, W., "Alloys SS316 and Hastelloy-C276 in Supercritical CO2 at High Temperature," *Oxidation of Met*als, Vol. 84, (2015), 585–606.

[10] Pint B. A., Keiser, J. R., "Initial Assessment of Ni-Base Alloy Performance in 0.1 MPa and Supercritical CO_2," *JOM*, Vol. 67, (2015), 2615-2620.

[11] Dheeradhada, V., Thatte, A., Karadge, M., Drobnjak, M., "Corrosion of Supercritical CO_2 Turbomachinery Components," in Proceedings of the EPRI International Conference on Corrosion in Power Plants, Oct. 2016, San Diego, CA.

[12] Pint B. A., Brese, R. G., "High-Temperature Materials," in Fundamentals and Applications of Supercritical Carbon Dioxide Based Power Cycles, K. Brun and P. Friedman, eds., Elsevier, London, (2017), pp.67-104.
[13] Pint, B. A., Brese, R. G., Keiser, J. R., "Effect of Pressure on Supercritical CO_2 Compatibility of Structural Alloys at 750°C," *Materials and Corros*ion, Vol. 68, (2017), 151-158.
[14] Oleksak, R. P., Tylczak, J. H., Carney, C. S., Holcomb, G. R., Dogan, O. N., "High-Temperature Oxidation of Commercial Alloys in Supercritical CO_2 and Related Power Cycle Environments," *JOM*, Vol. 70, (2018), 1527-1534.
[15] Olivares, R. I., Young, D. J., Nguyen, T. D., Marvig, P., "Resistance of High-Nickel, Heat-Resisting Alloys to Air and to Supercritical CO_2 at High Temperatures," *Oxidation of Metals*, Vol. 90, (2018), pp. 1-25.
[16] Pint, B. A., Pillai, R., Lance M. J., Keiser, J. R., "Effect of Pressure and Thermal Cycling on Long-Term Oxidation in CO_2 and Supercritical CO_2" *Oxidation of Metals*, Vol. 94, (2020), pp. 505–526.
[17] Mahaffey, J., Adam, D., Brittan, A., Anderson, M., Sridharan, K., "Corrosion of Alloy Haynes 230 in High Temperature Supercritical Carbon Dioxide with Oxygen Impurity Additions," *Oxidation of Metals*, Vol. 86, (2016), 567-580.
[18] Pint, B. A., Lehmusto, J., Lance M. J., Keiser, J. R., "The Effect of Pressure and Impurities on Oxidation in Supercritical CO_2," *Materials and Corros*ion, Vol. 70, (2019), 1400-1409.
[19] Oleksak, R. P., Carney, C. S., Dogan, O. N., "Effect of pressure on high-temperature oxidation of Ni alloys in supercritical CO_2 containing impurities," *Corrosion Science*, Vol. 215, (2023), 111055.
[20] Pint, B. A., Lance M. J., Pillai, R., Keiser, J. R., "Effect of Impurities on the Compatibility of Steels in Supercritical CO_2 at 450°-650°C," *Journal of Engineering for Gas Turbines & Power*, Vol. 146, (2024), p. 091007. doi.org/10.1115/1.4064585.
[21] McCoy, H. E., "Type 304 Stainless Steel vs Flowing CO_2 at Atmospheric Pressure and 1100-1800°F," *Corros*ion, Vol. 21, (1965), pp. 84-94.
[22] Gong, Y., Young, D. J., Kontis, P. Chiu, Y. L., Larsson, H., Shin, A., Pearson, J. M., Moody, M. P., Reed, R. C., 2017, "On the breakaway oxidation of Fe9Cr1Mo steel in high pressure CO_2," *Acta Materialia*, Vol. 130, (2017), 361-374.
[23] Sarrade, S., Férona, D., Rouillard, F., Perrin, S., Robin, R., Ruiz, J.-C., Turc, H.-A., "Overview on corrosion in supercritical fluids," *Journal of Supercritical Fluids*, Vol. 120 (2017) 335–344.
[24] Furukawa, T., Inagaki, Y., Aritomi, M., "Compatibility of FBR structural materials with supercritical carbon dioxide," *Progress in Nuclear Energy*, 5 Vol. 3, (2011), pp. 1050–1055.
[25] Tan, L. Anderson, M., Taylor, D., Allen, T. R., "Corrosion of austenitic and ferritic-martensitic steels exposed to supercritical carbon dioxide," *Corrosion Sci*ence, Vol. 53, (2011), 3273-3280.
[26] Cao, G., Firouzdor, V., Sridharan, K., Anderson, M., Allen, T. R., "Corrosion of austenitic alloys in high temperature supercritical carbon dioxide," *Corrosion Sci*ence, Vol. 60, (2012), 246-255.
[27] Pint, B. A., Su, Y.-F., Lance M. J., Pillai, R., Keiser, J. R., "Internal Carburization and Scale Formation on Austenitic Steels in Supercritical Carbon Dioxide," *Materials at High Temp*erature, Vol. 40, (2023), pp. 308-317.
[28] Viswanathan, R., Shingledecker, J., Purgert, R., "Evaluating Materials Technology for Advanced Ultrasupercritical Coal-Fired Plants," *Power*, Vol. *154*(8), (2010), pp. 41-45.
[29] Shingledecker, J. P., Pint, B. A., Sabau, A. S., Fry, A. T., Wright, I. G., "Managing Steam-Side Oxidation and Exfoliation in USC Boiler Tubes," *Advanced Materials & Processing*, Vol. 171 (1), (2013), pp. 23-25.
[30] Pint B. A., "High-Temperature Corrosion in Fossil Fuel Power Generation: Present and Future," *JOM*, 65, (2013), pp. 1024-1032.
[31] Pint, B. A., "High temperature compatibility of structural alloys with supercritical and subcritical CO_2," *Interface*, Vol. 30, (2021), pp. 67-71.

[32] Pint, B. A., Pillai, R., Keiser, J. R., 2023, "Evaluation of Coatings to Improve Steel Compatibility in Supercritical CO_2" AMPP Paper C2023-19207, Houston, TX, to be presented at AMPP Annual, March 2023, Denver, CO.
[33] Pint, B. A., Pillai, R., Lance, M. J., Keiser, J. R., "Coated and Uncoated Steel Compatibility in Supercritical CO_2 at 450°-650°C," in Proceedings of the 8th International Symposium on Supercritical CO_2 Power Cycles, San Antonio, TX, February 2024, Paper #113.
[34] Pint, B. A., Pillai, R., Su, Y.-F., Lance, M. J., Keiser, J. R., "Evaluation of Coated Steels in Supercritical CO_2," *Mater. Corros.*, in press, (2024). doi.org/10.1002/maco.202314271.
[35] Pint, B. A., Zhang, Y., "Performance of Al-rich Oxidation Resistant Coatings for Fe-Base Alloys," *Materials and Corros*ion, Vol. 62, (2011), pp. 549-560.
[36] López, A. J., Proy, M., Utrilla, V., Otero, E., Rams, J., "High-temperature corrosion behavior of Ni–50Cr coating deposited by high velocity oxygen–fuel technique on low alloy ferritic steel," *Materials and Design* Vol. 59, (2014), pp. 94–102.
[37] Agüero, A., Baraibar, I., González, V., Muelas, R., Plana, D., "Corrosion Resistance of Novel Coatings on Ferritic Steels for Oxycombustion–Supercritical Steam Boilers: Preliminary Results," *Oxidation of Metals*, Vol. 85, (2016), pp. 263–281.
[38] Nguyen, T. D., Peng, X., Zhang, J. Q., Young, D. J., "Corrosion resistance of chromised and aluminised coatings in wet CO_2 gas at 650°C," *Surface and Coatings Technology*, Vol. 316, (2017), pp. 226–238.
[39] Kim, C., Kim, S. H., Cha, J.-H., Jang, C., Kim, T. K., "Cr diffusion coating to improve the corrosion resistance of an ODS steel in super-critical carbon dioxide environment," *Surface and Coatings Technology*, Vol. 374, (2019), 666-673.
[40] Brittan, A. M., Mahaffey, J. T., Colgan, N. E., Elbakhshwan, M., Anderson, M. H., "Carburization resistance of cu-coated stainless steel in supercritical carbon dioxide environments," *Corrosion Science*, Vol. 169, (2020), 108639.
[41] Kim, S. H., Kim, C., Cha, J.-H., Jang, C., "Corrosion Behavior of Si Diffusion Coating on an Austenitic Fe-Base Alloy in High Temperature Supercritical-Carbon Dioxide and Steam Environment," *Coatings*, Vol. 10, (2020), pp. 493.
[42] Meissner, T. M., Gregoire, B., Montero, X., Miller, E., Maier, J., Galetz, M. C., "Long-Term Corrosion Behavior of Cr Diffusion Coatings on Ferritic-Martensitic Superheater Tube Material X20CrMoV12-1 under Conditions Mimicking Biomass (Co-)firing," *Energy & Fuels*, Vol. 34, (2020), pp. 10989-11002.
[43] More, K. L., Tortorelli, P. F., Ferber, M. K., Keiser, J. R., "Observations of Accelerated Silicon Carbide Recession by Oxidation at High Water-Vapor Pressures," *Journal of the American Ceramic Society*, Vol. 83, (2000), pp. 211-213.
[44] Terrani, K. A., Pint, B. A., Parish, C. M., Silva, C. M., Snead, L. L., Katoh, Y., "Silicon Carbide Oxidation in Steam up to 2 MPa," *Journal of the American Ceramic Society*, Vol. 97, (2014), pp. 2331-2352.
[45] Pieraggi, B., "Calculations of Parabolic Reaction Rate Constants," *Oxidation of Met*als Vol. 27, (1987), pp. 177-185.
[46] Pint, B. A., Keiser, J. R., "Exploring Material Solutions for Supercritical CO_2 Applications above 800°C," *Oxidation of Metals*, Vol. 98, (2022), pp. 545-559.
[47] Pint, B. A., Pearson, S. R., De Las Casas Aranda, R., Lance, M. J., Raiman, S. S., Kung, S. C., "Water Chemistry and Pressure Effects on Steam Oxidation of Ferritic and Austenitic Steels," in Proceedings of the Joint EPRI – 123HiMAT International Conference on Advances in High Temperature Materials, J. Shingledecker and M. Takeyama eds., ASM International, Materials Park, OH, (2019), pp.939-947.
[48] Gheno, T., Monceau, D., Zhang, J., Young, D. J., "Carburisation of Ferritic Fe-Cr Alloys by Low Carbon Activity Gases," *Corrosion Science*, Vol. 53, (2011), pp. 2767-2777.
[49] Dryepondt, S., Lehmusto, J., Pint, B. A., "Effect of Annealing and Supercritical CO_2 Exposure at 750 °C on the Tensile Properties of Stainless Steel and Ni-based Structural Alloys," *Materials and Corrosion*, Vol. 73, (2022), pp. 497-512.